

PCCP

Physical Chemistry Chemical Physics

Accepted Manuscript

This article can be cited before page numbers have been issued, to do this please use: N. Hadilou, S. souri, A. Navid, R. Sadighi-Bonab, A. Anvari and B. Palpant, *Phys. Chem. Chem. Phys.*, 2020, DOI: 10.1039/D0CP01509A.



This is an Accepted Manuscript, which has been through the Royal Society of Chemistry peer review process and has been accepted for publication.

Accepted Manuscripts are published online shortly after acceptance, before technical editing, formatting and proof reading. Using this free service, authors can make their results available to the community, in citable form, before we publish the edited article. We will replace this Accepted Manuscript with the edited and formatted Advance Article as soon as it is available.

You can find more information about Accepted Manuscripts in the [Information for Authors](#).

Please note that technical editing may introduce minor changes to the text and/or graphics, which may alter content. The journal's standard [Terms & Conditions](#) and the [Ethical guidelines](#) still apply. In no event shall the Royal Society of Chemistry be held responsible for any errors or omissions in this Accepted Manuscript or any consequences arising from the use of any information it contains.

Cite this: DOI: 00.0000/xxxxxxxxxx

An Optimal Architecture of Magneto-Plasmonic Core-Shell Nanoparticles for Potential Photothermal Applications[†]

Naby Hadilou,^{ab‡} Somayeh Souiri,^{b‡} Ali Navid Khoshgenab,^a Rasoul Sadighi Bonabi,^{b*} Abbas Anvari^b and Bruno Palpant^cReceived Date
Accepted Date

DOI: 00.0000/xxxxxxxxxx

In this work, the optical response of $Fe_3O_4@Au$ and $Fe_3O_4@Ag$ are comprehensively investigated using the Discrete Dipole Approximation. It is found that the resonance wavelength as well as absorption efficiency strongly depend on the composition of core and shell, geometry of nanoparticle, core to particle volume ratio, core radius and shell thickness. The strongest impact is due to the shell material, the shape of nanoparticle and their combination. When the composition of the shell is changed from gold to silver, instead of one fundamental resonance peak the absorption spectrum shows two ones corresponding to the bonding plasmon mode at nanoparticle-environment interface and antibonding mode at core-shell interface. The results also reveal a much higher tunability of the resonance wavelength as well as larger enhancement of the absorption efficiency as the spherical nanoparticle stretches to prolate ellipsoidal shape. Furthermore, higher order plasmon modes appear in the absorption spectrum of prolate nanoparticles with large aspect ratio. Existence of several plasmon modes together with wide tunability make these nanoparticles good candidates for applications where two or more simultaneous absorption bands at different frequencies are required. These results might motivate the experimentalists to optimize the synthesis of magnetic-plasmonic core-shell NPs in different applications as far as absorption is concerned.

1 Introduction

Recently, there has been a considerable effort to design and develop more sensitive and efficient plasmonic nanohybrid structures for a number of applications such as biosensors^{1,2}, catalysis³, photothermal cancer therapy⁴⁻⁶ and controllable drug delivery⁷⁻⁹. A main advantage of using noble metals is to benefit from their optical properties which are determined by the Localized Surface Plasmon Resonance (LSPR).

LSPR represents the collective oscillation of conduction electrons at the interface between a metal nanoparticle (NP) and its dielectric surrounding when excited by an incident electromagnetic field. The main result of LSPR is the strong light confinement which leads to local electric field enhancement near the metal surface. Usually, the optical response of nanostructures is investigated in terms of scattering and absorption. The scattering and absorption spectra of these NPs always show maxima at

LSPR frequencies, with the optical response being highly sensitive to the nanostructure's morphology, composition, size, shape and geometry. Depending on the NP size, the incident electromagnetic wave can be either scattered or absorbed. The absorption process dominates for NPs less than ~ 50 nm in diameter while the scattering is the main process with larger particles. In other words, while large NPs are proper candidates for applications which need high scattering, small NPs convert the absorbed light into heat and act as miniature heat sources¹⁰. Heat generation in plasmonic NPs opens a new field of thermoplasmonics with focusing on emerging application such as nano-optics and nanothermodynamics¹¹.

On the other side, magnetic NPs have attracted intensive attention due to their great number of applications such as magnetic resonance imaging¹² and magnetic guided drug delivery¹³. Magnetite (Fe_3O_4) is the most commonly used material for magnetic NPs in biomedical applications which can be easily synthesized in different sizes and morphologies¹⁴⁻¹⁶.

To tune the LSPR over a wide range of the electromagnetic spectrum, various geometries have been investigated. Among numerous candidates, core-shell NPs have shown more promise in different applications as a result of their outstanding bifunctional

^a Department of Laser and Optical Engineering, University of Bonab, Bonab, Iran.^b Department of Physics, Sharif University of Technology, Tehran, Iran.^c Université Paris-Saclay, CNRS, ENS Paris-Saclay, CentraleSupélec, LuMIn, 91190 Gif-sur-Yvette, France.[†] These authors contributed equally to this work.

properties. High stability, low reactivity and surface modification are some of the important benefits of these NPs¹⁷. In addition, the different chemical and physical properties of the core and shell parts make this structure more attractive^{18–20}. Moreover, compared to single NPs and their bulk materials, an extra degree of freedom in LSPR is provided using a core-shell structure²¹. As a result, the core-shell NPs exhibit more flexibility to tune the plasmonic resonance over a wide range of wavelengths. Core-shell NPs composed of a magnetic core with a plasmonic metal shell would combine the magnetic and plasmonic properties. The magnetic core introduces a triggering ability in the presence/absence of external magnetic field, and the plasmonic shell is responsible for light absorption at the LSPR frequency and conversion to heat. The best choices for shell are gold and silver metals due to their outstanding optical properties in the wide range of electromagnetic waves from UV to near IR (200–1200 nm)^{22,23}.

The well-established methods to synthesize magneto-plasmonic core-shell NPs are reported that allow good control over the shape and size of the NPs^{7,19,24}. Moreover, these NPs are subject of many theoretical studies aiming to tune the resonance position and enhance the absorption efficiency^{25–27}. In spite of the literature in this field, to the best of our knowledge, further studies considering simultaneously all important parameters for magnetite core coated by gold or silver with different shapes are still necessary.

In this paper, the optical properties of core-shell NP are comprehensively investigated by applying dipolar model theory and using the Discrete Dipole Approximation method. The results indicate that the LSPR frequency is strongly influenced by the NP shape and can be tuned by stretching or flattening the nanosphere. In addition, the effect of aspect ratio, core diameter and shell thickness are thoroughly analyzed. Moreover, since LSPR frequency and absorption efficiency are directly affected by NP composition, both silver and gold are considered as the metallic shell. Two plasmon modes are generated in a core-shell structure: a bonding mode at the NP-environment interface and an antibonding mode between the magnetic core and the plasmonic shell. The existence of a bonding mode for $Fe_3O_4@Au$ and both bonding and antibonding modes for $Fe_3O_4@Ag$ is demonstrated. At the same time, the LSPR peak shift of core-shell NPs with different geometric parameters is analyzed.

2 Theoretical Method

One of the most extensively used structures for core-shell NP is a spheroid. The spheroid is an ellipsoid with two equal semi-diameters that can look like either a stretched (prolate) or a flattened (oblate) sphere. The spheroid is defined by two axes, minor and major, denoted by a and c , respectively. For an oblate spheroid, two minor axes have the same size while two major axes equal for prolate; in other words, for oblate $a = b < c$ and for prolate $a = b > c$. If the length of the major axis is the same as the length of the minor axis ($c = a$), the spheroid will be a sphere. The spheroidal geometry enables to study the effect of shape and aspect ratio (AR) of NPs besides their size and composition. Note that the AR of spheroids is defined as the ratio of major and the minor axis ($\frac{c}{a}$).

To calculate the absorption efficiency of NP, dipolar model (analytical approach) for spherical NPs and discrete dipole approximation (numerical approach) for spheroidal NPs are utilized.

2.1 Absorption efficiency for spherical nanoparticle

In dipolar model, when a NP is illuminated, the external field induces a dipole moment inside the NP proportional to the field $\vec{p} = \alpha \vec{E}_0$, where E_0 is the external electric field amplitude experienced by the particle and α is the effective polarizability of NP. Once the polarizability of the target structure is known, the absorption cross-section can be calculated.

The polarizability of an ellipsoidal core-shell NP (α_i) along the principal axes ($i = a, b, c$) is given by the following equation^{28–30}:

$$\alpha_{i,NP} = V \times$$

$$\frac{(\epsilon_{Sh} - \epsilon_m)[\epsilon_{Sh} + L_i^{Co}(\epsilon_{Co} - \epsilon_{Sh})] + f[\epsilon_{Sh} + L_i^{Sh}(\epsilon_m - \epsilon_{Sh})](\epsilon_{Co} - \epsilon_{Sh})}{[\epsilon_m + L_i^{Sh}(\epsilon_{Sh} - \epsilon_m)][\epsilon_{Sh} + L_i^{Co}(\epsilon_{Co} - \epsilon_{Sh})] + fL_i^{Sh}(1 - L_i^{Sh})(\epsilon_{Sh} - \epsilon_m)(\epsilon_{Co} - \epsilon_{Sh})} \quad (1)$$

where ϵ_{Co} , ϵ_{Sh} and ϵ_m are the dielectric constants of the core, shell and surrounding medium, respectively. $V = \frac{4}{3}\pi a^2 c$ is the volume of the NP and f represents the core to particle volume ratio. L_i^{Co} and L_i^{Sh} are the geometrical factors of the core and shell. The geometrical factors of sphere, oblate and prolate along major axis ($i = c$) are defined as follows:

$$L_{c,sphere} = \frac{1}{3} \quad (2)$$

$$L_{c,oblate} = \frac{1 + g_{obl}^2}{g_{obl}^2} \left(1 - \frac{1}{g_{obl}} \tan^{-1} g_{obl}\right) \quad (3)$$

$$L_{c,prolate} = \frac{1 - g_{pr}^2}{g_{pr}^2} \left(\frac{1}{2g_{pr}} \ln \frac{1 + g_{pr}}{1 - g_{pr}} - 1\right) \quad (4)$$

$g_{pr} = -g_{obl} = 1 - (AR)^2$. The geometrical factors along minor axes ($i = a, b$) is $L_i = \frac{1}{2}(1 - L_c)$.

It is well-known that the resonance appears when the the Fröhlich condition is satisfied. This corresponds to the zero value of the real part of the denominator in Eq. 1³¹.

$$C_{abs} = k \operatorname{Im}[(\alpha_a + \alpha_b + \alpha_c)/3] \quad (5)$$

where k is the wave-number.

Substituting Eq. 2 in Eq. 1, the polarizability of the spherical core-shell NP is obtained:

$$\alpha_{core-shell} = 4\pi \frac{(\epsilon_{Sh} - \epsilon_m)(\epsilon_{Co} + 2\epsilon_{Sh}) + f(\epsilon_{Co} - \epsilon_{Sh})(\epsilon_m + 2\epsilon_{Sh})}{(\epsilon_{Sh} + 2\epsilon_m)(\epsilon_{Co} + 2\epsilon_m) + 2f(\epsilon_{Sh} - \epsilon_m)(\epsilon_{Co} - \epsilon_{Sh})} \quad (6)$$

According to Eq. 1, the polarizability of spheroidal core-shell NPs and thus the resonance condition are extremely dependent on these factors: (1) composition of the core and the shell; It is clear that the polarizability is sensitive to permittivity of core, shell and environment. (2) core: particle volume ratio; f can be altered by changing both the core diameter and the shell thickness. (3) shape and geometry of NP; the resonance condition is strongly sensitive to both core and shell geometrical factor. Therefore, aspect ratio adjustment leads to modify the absorption spec-

trum. As a result, the absorption spectrum can be tuned by modification of shell material, core diameter, shell thickness, shape and aspect ratio. In this paper, all these parameters are investigated and the corresponding absorption efficiency is calculated.

2.2 Absorption efficiency for spheroidal nanoparticle

To calculate the absorption of light by NPs, numerous different numerical techniques are proposed. Among them, one of the most powerful and flexible method that can be applied to NPs of arbitrary geometry and composition is the Discrete Dipole Approximation (DDA)^{32,33}. In this method, the NP is considered as a cubic array of point dipoles. The polarizability of each NP (α_i) is determined by interacting these dipoles with each other and with the incident field.

$$\vec{p}_i = \alpha_i (\vec{E}_{i,inc} + \vec{E}_{i,ind}) = \alpha_i \left\{ \vec{E}_0 e^{i\vec{k} \cdot \vec{r}_i} - \sum_{j \neq i} \vec{A}_{ij} \cdot \vec{p}_j \right\} \quad (7)$$

\vec{p}_i is the dipole moment of the i th element at \vec{r}_i . The incident field and the field radiated by all neighboring dipoles represent by $\vec{E}_{i,inc}$ and $\vec{E}_{i,ind}$, respectively. \vec{A}_{ij} is a 3×3 tensor:

$$\vec{A}_{ij} \cdot \vec{p}_j = \frac{e^{ikr_{ij}}}{r_{ij}^3} \{ k^2 \vec{r}_{ij} \times (\vec{r}_{ij} \times \vec{p}_j) + \frac{(1 - ikr_{ij})}{r_{ij}^2} [r_{ij}^2 \vec{p}_j - 3\vec{r}_{ij}(\vec{r}_{ij} \cdot \vec{p}_j)] \} \quad (8)$$

Here, $\vec{r}_{ij} = \vec{r}_i - \vec{r}_j$ is the distance between two particles of i and j . As coordinates and polarizabilities of the individual dipoles are known, the absorption cross-section (C_{abs}) of the whole structure can be determined.

$$C_{abs} = \frac{4\pi k}{E_0^2} \sum_{i=1}^N \{ \text{Im}[\vec{p}_i \cdot (\alpha_i^{-1})^* \vec{p}_i] - \frac{2}{3} k |\vec{p}_i|^2 \} \quad (9)$$

The problem is fully characterized by the geometric distribution of the polarizable points, the polarizability of each point, and the incident electromagnetic wave. The polarizability α_i is chosen according to some prescription. A polarizability assigned to each point is given by the Lattice Dispersion Relation (LDR)³³⁻³⁵:

$$\alpha_i^{LDR} = \frac{\alpha_i^{CM}}{1 + \alpha_i^{CM} [b_1 + b_2 \epsilon_i + b_3 S \epsilon_i] (k^2/d)} \quad (10)$$

S , b_1 , b_2 and b_3 are the coefficients of the expansion to a third order in k to incorporate radiation effects, and α_i^{CM} is the polarizability given by the well-known Clausius-Mossotti relation^{36,37}:

$$\alpha_i^{CM} = \frac{3d^3}{4\pi} \frac{\epsilon_i - 1}{\epsilon_i + 2} \quad (11)$$

Let us underline that the accuracy of the calculation is sensitive to the number of dipoles (i.e. dipole separation). The only limitation of DDA is that the dipole separation must be small compared to not only any structural lengths of NP, but also the wavelength of incident light. DDSCAT 7.3 is a freely available open-source FORTRAN-90 software package applying the DDA method to calculate absorption of electromagnetic waves on targets with arbitrary geometries and complex optical indices^{33,38,39}. Here, the optical properties of spheroidal NPs including nanoparticle with the shape of an oblate and prolate are fully explored using

DDSCAT 7.3.

2.3 Simulation

The purpose of this paper is to get more efficient magneto-plasmonic core-shell NPs for photothermal applications. It has been proven that the NPs should be small enough in photothermal and biomedical applications, typically 10-100 nm or smaller⁴⁰⁻⁴². On the other hand, the lower bounds should take account of fabrication control achievement to get realistic and feasible samples. In addition, there is another limitation to choosing NP's size. DDA breaks down as the size of NP and the shell thickness significantly decrease. As a result, the size of all NPs in this work is considered in the range of 10-100 nm.

From Eq. 6 and Eq. 10, it is apparent that the polarizability of NP in both methods (dioplar model and DDA) contains various parameters that have their own significant. Out of these parameters, the dielectric constant is one of the most important parameters to understand the optical properties of metal nanoparticle. Drude-Lorentz model gives the size dependent dielectric function of the NP as⁴³⁻⁴⁶:

$$\epsilon(\omega) = \epsilon_{bulk} + \frac{\omega_p^2}{\omega^2 + i\omega\gamma_{bulk}} - \frac{\omega_p^2}{\omega^2 + i\omega(\gamma_{bulk} + \frac{v_F}{R})} \quad (12)$$

ϵ_{bulk} is the bulk metal dielectric constant, ω_p is the plasma frequency ($\omega_p^{Au} = 9$ eV and $\omega_p^{Ag} = 8.9$ eV) and ω is the angular frequency of the incident field. γ_{bulk} is the electron collision damping in the metal ($\gamma_{bulk}^{Au} = 0.066$ eV and $\gamma_{bulk}^{Ag} = 0.018$ eV). v_F is the electron's Fermi velocity ($v_F^{Au} = 1.4 \times 10^6$ m/s and $v_F^{Ag} = 1.39 \times 10^6$ m/s) and R is the effective mean free path. The dielectric constant values of gold and silver were taken from Johnson and Christy⁴⁷. The missing data were interpolated from the available experimental data by the cubic spline interpolation method. The dielectric constant values of magnetite were taken from literature^{48,49}. In the spectral range 200-1200 nm, the dielectric constant of Fe_3O_4 is approximately constant; $\epsilon_{Co} = 2.325 + 0.1265i$.

The refractive index of the surrounding medium is set to $n_m = 1.48$. In drug delivery applications, it is common to encapsulate the core-shell NPs with bio-compatible polymers. The polymeric part acts as a controllable valve and is responsible for loading and releasing drugs⁷. Usually, the size of polymer part is much larger than the NP size. Therefore, it can be assumed that the NP is embedded in a polymeric environment.

Each DDA simulation contains between 100,000 and 900,000 dipoles to ensure that accurate results are obtained. Since, the unpolarized light is used in the experiment, all absorption spectra are averaged over two orthogonal polarizations, which approximate the response of the NP to unpolarized light. Note that all absorption spectra are plotted in terms of absorption efficiency. Absorption efficiency is defined as the ratio of an absorption cross-section (C_{abs}) to a NP's geometric cross-sectional area;

$$Q_{abs} = \frac{C_{abs}}{\pi a_{eff}^2} \quad (13)$$

where a_{eff} is the effective radius of NP.

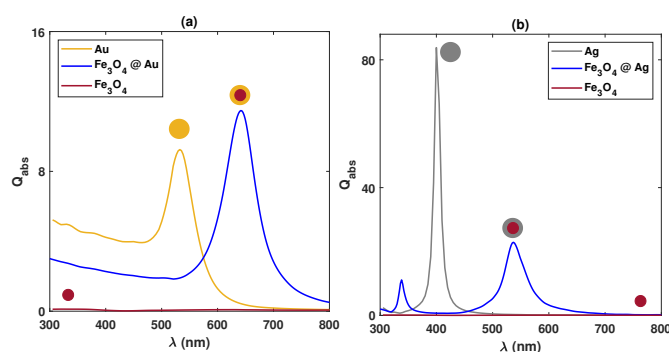


Fig. 1 The absorption spectra of (a) $Fe_3O_4@Au$ and (b) $Fe_3O_4@Ag$ core-shell NPs. The total diameter of each NP is 24 nm. For core-shell NPs, the shell thickness is 4 nm.

3 Results and Discussion

In this section, the optical properties of the magneto-plasmonic core-shell NPs with two different plasmonic metals (gold and silver) are fully investigated.

Here, the absorption spectra of $Fe_3O_4@Au$ and $Fe_3O_4@Ag$ inside the polymeric environment with a refractive index of 1.48 are studied and compared. Also, the effect of geometry and size of these NPs are comprehensively explored. To achieve wide tunability in LSPR, three core-shell spheroidal structures with both silver and gold shells are considered. For all cases, the effect of the size of NP, core radius and shell thickness on the absorption efficiency is analyzed.

3.1 Effect of Shell Composition.

To investigate the effect of the metallic shell material, the absorption spectra of 24 nm diameter core-shell NPs with 4 nm metal shell (Au and Ag) and 16 nm magnetite core in the polymer environment were calculated. The simulation results reported in Fig. 1 indicate that there is one pronounced peak in the absorption spectrum of pure Au and pure Ag spherical NPs at 532 nm and 400 nm, respectively. For a pure Fe_3O_4 NP, there is no LSPR peak. Compared to a pure Au NP, LSPR peak of $Fe_3O_4@Au$ is redshifted to 641 nm and its intensity is enhanced by about 25 percent. In the contrary, in case of Ag shell, the existence of two distinct absorption peaks is the most significant feature of $Fe_3O_4@Ag$: a redshifted peak with higher absorption efficiency located at 537 nm and a blueshifted peak with lower absorption efficiency positioned at 338 nm. Compared to a pure Ag NP, the intensity of the former and latter is reduced by about 85% and 70 %, respectively.

According to the plasmon hybridization model⁵⁰, for core-shell nanostructures, two internal boundaries exist; inner and outer interface of the metal shell. The electromagnetic wave induces plosmon mode at these two boundaries, one at the core-shell interface and another at the shell-environment interface. These two modes interact with each other and lead to splitting the plasmon mode into two new resonance modes; Bonding Mode (BM) and Antibonding Mode (ABM). It is possible that the coupling between the antibonding mode and the electromagnetic wave is very weak which makes it too difficult to observe in the absorption spec-

trum^{51,52}. From Fig. 1, the bonding mode (BM) appears for both Au and Ag shell, while the antibonding mode (ABM) exists only for $Fe_3O_4@Ag$.

To explain this observation, the effective dielectric constant of spherical core-shell $Fe_3O_4@Au$ and $Fe_3O_4@Ag$ is also calculated using internal homogenization scheme and plotted in Fig. 2(c)⁵³. In this scheme, the core-shell spherical NP is replaced by a single spherical NP of the same size (or outer radius) but with a single effective permittivity filling the entire sphere. i.e. a single effective permittivity is assigned to coated spheres. Under the quasi-static approximation, only the dipolar terms are important and so as long as the two particles possess the same polarizability they will interact with any excitation in an identical manner. Equating the polarizability of a core-shell spherical NP (Eq. 6) and a single spherical NP ($\alpha_e = 4\pi a^3(\epsilon - \epsilon_m)/(\epsilon + 2\epsilon_m)$) yields the following equation for the effective permittivity.

$$\epsilon_e = \epsilon_{Sh} \frac{a^3(\epsilon_{Co} + 2\epsilon_{Sh}) + 2b^3(\epsilon_{Co} - \epsilon_{Sh})}{a^3(\epsilon_{Co} + 2\epsilon_{Sh}) - b^3(\epsilon_{Co} - \epsilon_{Sh})} \quad (14)$$

b^3/a^3 is the filling fraction of the core material. Note that the effective permittivity of core-shell NP depends on filling factor. Data plotted in Fig. 2(b) is related to the NP with core radius of 8 nm and shell thickness of 4 nm. Using Eq. 14 and taking effective dielectric constant for $Fe_3O_4@Au$ and $Fe_3O_4@Ag$ that are plotted in Fig. 2(b), the polarizability of these NPs are plotted in Fig. 2(c). As mentioned, the polarizability experiences a resonance condition when the real part of the denominator in Eq. 14 vanishes. Fig. 2(c) denotes that the polarizability experiences two resonant conditions for $Fe_3O_4@Ag$ around 340 nm and 540 nm, while Fröhlich condition for $Fe_3O_4@Au$ is only satisfied at 640 nm. Aforementioned, coupling between antibonding mode and EM wave for $Fe_3O_4@Au$ is too weak to affect the absorption spectrum.

For better understanding, the electric field distribution near the NPs is also computed. The electric field distribution for NPs is depicted in Fig. 3 both at the lower and higher energy modes at the corresponding resonance wavelengths. For the resonance at long wavelengths (641 nm for Au shell and 538 nm for Ag shell), the electric field is mainly concentrated at the outer interface, whereas the concentration of this field is at the inner interface for shorter wavelength (338 nm for Ag shell). It is also observed that the electric field enhancement of $Fe_3O_4@Ag$ is higher than for $Fe_3O_4@Au$. The normalized electric field maximum for the first one is around 18, while for $Fe_3O_4@Au$ it reaches about 9.

In terms of heat generation, the temperature increase (ΔT) at the given distance from NP (R) is calculated. The calculations are done for NP illumination of resonance frequencies. At steady state condition, the heat generated by a spherical NP in a homogeneous surrounding medium is obtained as following⁵⁴:

$$\Delta T = \frac{C_{LSPR}^{abs} I}{4\pi\kappa R} \quad (15)$$

I is the illuminating power density of the light. κ is the thermal conductivity of the surrounding medium ($\kappa_{polymer} = 0.4 \text{ W.m}^{-1}.K^{-1}$) and R is the distance from the center of the sphere.

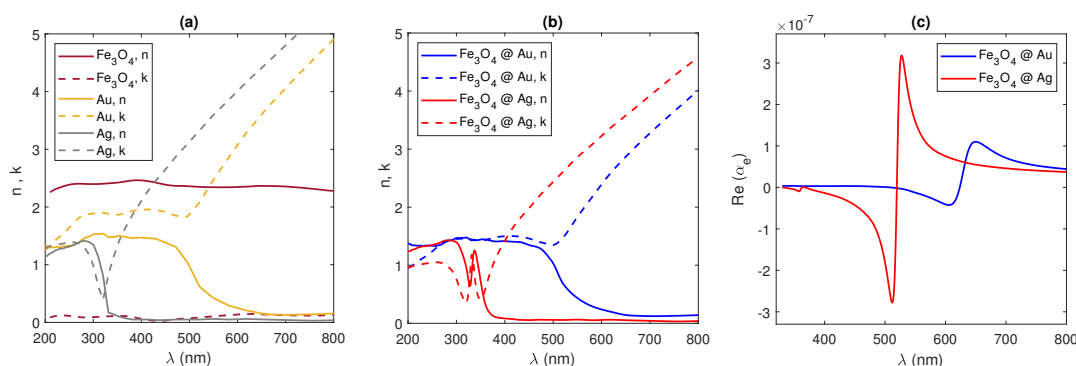


Fig. 2 Refractive index and extinction coefficient of (a) gold, silver, magnetite and (b) core-shell NPs ($Fe_3O_4@Au$ and $Fe_3O_4@Ag$). (c) Real part of the polarizability of $Fe_3O_4@Au$ and $Fe_3O_4@Ag$ core-shell NPs with respect to the wavelength of the driving field. The core diameter is 16 nm and the shell thickness is 4 nm.

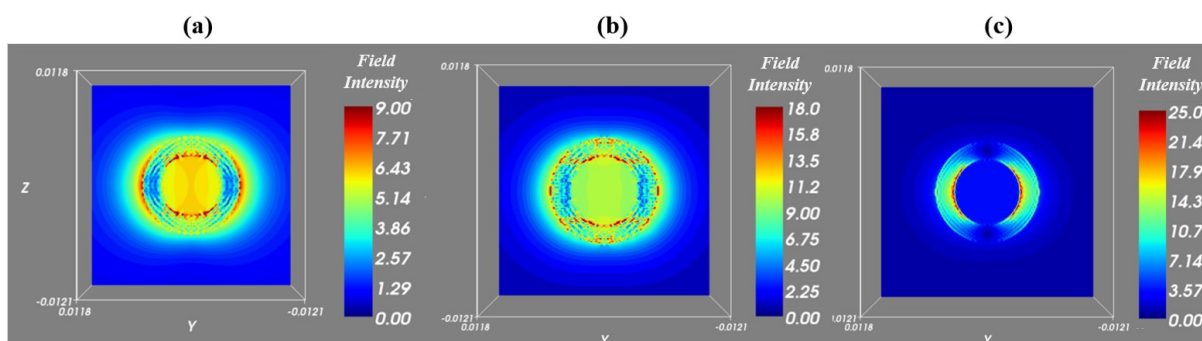


Fig. 3 Electric field distribution of the (a) $Fe_3O_4@Au$ at 641 nm, (b) $Fe_3O_4@Ag$ at 538 nm and (c) $Fe_3O_4@Ag$ at 338 nm. The core radius and shell thickness are 8 nm and 4 nm, respectively.

According to Eq. 15, the temperature increase generated by $Fe_3O_4@Ag$ is much higher than that of $Fe_3O_4@Au$. For the NPs in Fig. 1, $\Delta T_{Ag} \approx 2.5\Delta T_{Au}$.

3.2 Effect of filling factor.

The impact of the filling factor (f) on the tunability of the resonance peak as well as the absorption efficiency is investigated by three different ways: (1) Simultaneous change of core radius and shell thickness while the total size of the NP remains constant, (2) modification of core radius when the shell thickness is unchanged and (3) shell thickness adjustment at fixed core radius. Here, we just follow the first way to demonstrate the filling factor effect on the LSPR position of spherical NPs. Later, we will go on studying the effect of f on the resonance position of all types of spheroidal NPs (spherical oblate and prolate) through the two other ways.

Fig. 4 reports the absorption spectra of $Fe_3O_4@Au$ and $Fe_3O_4@Ag$ where the filling factor is varied by keeping the NP diameter fixed at 24 nm. According to Fig. 4(a), the BM LSPR peak of $Fe_3O_4@Au$ moves toward the longer wavelength with an increase in core radius corresponding to the decrease in shell thickness. In other words, by increasing the filling factor, a redshift of the resonance peak is observed in the spectrum. The absorption efficiency is also increased. The effect of simultaneous change of core radius and shell thickness on the LSPR wavelength and its efficiency is reported in Fig. 4(c).

From Fig. 4(b), for $Fe_3O_4@Ag$, only one LSPR mode is observed in the absorption spectrum when the filling factor is too small (less than 2%). By increasing the filling factor, the interaction between the magnetite core and the silver shell leads to splitting of the peak into a bonding mode and an antibonding mode. The BM resonance is redshifted relative to pure silver NP, while the ABM resonance experiences a blueshift. With further increase of f , BM resonance significantly moves toward longer wavelengths. Despite the advantage of high resonance displacement, the absorption efficiency is reasonably reduced compared to the pure silver NP absorption. The position and efficiency of ABM, on the other hand, almost remains constant with a minimal blueshift. Fig. 4(d) provides the detail of the filling factor effect on LSPR wavelength and absorption of BM and ABM of $Fe_3O_4@Ag$.

3.3 Effect of Shape.

Here, the optical properties of NPs are calculated for three different spheroidal core-shell NPs including spherical, oblate and prolate NPs. In this regard, the core minor radius (a) is set to be 8 nm whereas the aspect ratio is increased from $\frac{1}{4}$ to 4. The shell thickness for all NPs is 4 nm. The absorption spectra of $Fe_3O_4@Au$ and $Fe_3O_4@Ag$ with different ARs in the polymeric environment with a refractive index of 1.48 are shown in Fig. 5.(a)-(b), respectively. When the shell material is silver, two resonance modes (BM

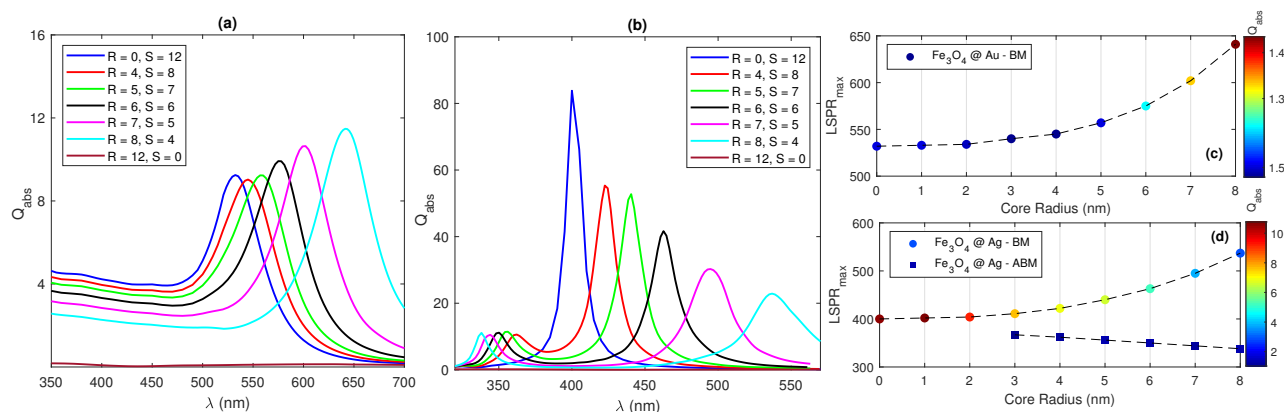


Fig. 4 Absorption spectra of (a) $\text{Fe}_3\text{O}_4@Au$ and (b) $\text{Fe}_3\text{O}_4@Ag$ with total diameter of 24 nm. Effect of varying the core radius and the shell thickness on the LSPR wavelength and its efficiency of (c) $\text{Fe}_3\text{O}_4@Au$ and (d) $\text{Fe}_3\text{O}_4@Ag$. The total radius of NPs is fixed at 12 nm.

and ABM) can be clearly observed in the absorption spectrum. As the shell metal changes to gold, one of the modes (ABM) disappears. This result is similar to what was discussed in the previous section.

For $\text{Fe}_3\text{O}_4@Au$, when the spherical NP becomes oblate, it has been found that the LSPR peak shifts toward shorter wavelengths and NP yields lower absorption efficiency. However, as the geometry of NP changes to prolate, the LSPR peak experiences a redshift and the absorption efficiency is significantly enhanced. The results reveal that the LSPR peak can be tuned from 609 nm to 932 nm and the absorption efficiency could be almost four times higher than as the AR of the spheroidal core-shell NP increases from $\frac{1}{4}$ to 4. For oblate $\text{Fe}_3\text{O}_4@Ag$, the LSPR peak at long wavelength, which originates from the bonding mode, experiences a blueshift, whereas the peak at short wavelength which arises from the antibonding mode experiences a redshift. As represented in Fig. 5.(b), the $\text{Fe}_3\text{O}_4@Ag$ NP with prolate shape displays opposite trends; The BM peak exhibits a redshift, whereas the ABM peak shows a blueshift. Based on the findings, by changing the AR from $\frac{1}{4}$ to 4, the BM peak can be considerably tuned from 504 nm to 858 nm and the ABM peak can be slightly adjusted from 336 nm to 344 nm. As compared to $\text{Fe}_3\text{O}_4@Au$, the absorption peak of $\text{Fe}_3\text{O}_4@Ag$ is higher due to the large absorption coefficient.

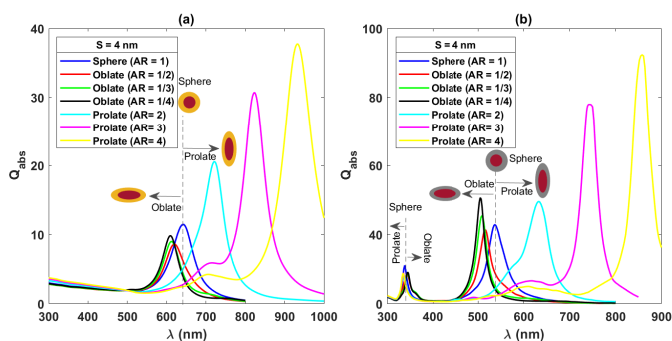


Fig. 5 Shape-dependent absorption spectra of core-shell (a) $\text{Fe}_3\text{O}_4@Au$ and $\text{Fe}_3\text{O}_4@Ag$. Minor radius and shell thickness of all NPs are $a = 8$ nm and $S = 4$ nm, respectively.

For both $\text{Fe}_3\text{O}_4@Au$ and $\text{Fe}_3\text{O}_4@Ag$ the absorption efficiency is increased as the NP shape changes from sphere to prolate. Therefore, NPs with prolate shape are predicted to be ideal candidates for photothermal applications due to high conversion of electromagnetic energy to thermal energy through the absorption process. Baffou *et al* also reported that the elongated, or sharp NPs generate higher heat in comparison with spherical NPs¹⁰. Fig. 5 indicates that the absorption efficiency of prolate is much higher than the one for sphere or oblate, which makes the NP with prolate shape much efficient miniature source of the heat. For a sphere or an oblate excited at its LSPR wavelength, the geometry of NP causes a major part of NP is not affected by the electromagnetic wave of light and only outer part of NP participates in the heat generation process. However, the inner part of NP gets closer to outer part by deforming the NP shape from sphere to prolate. As a result, almost whole volume of NP involves in the heat generation.

Another interesting outcome from Fig. 5 is the emergence of new peaks in the absorption spectra of both $\text{Fe}_3\text{O}_4@Au$ and $\text{Fe}_3\text{O}_4@Ag$ prolate NPs with large aspect ratio. The main reason is that the polarizability of spheroids strongly depends on its geometrical factor. The polarizability of an ellipsoidal NP (α_i) along the principal axes ($i = 1, 2, 3$) is given by Eq. 16²⁹:

$$\alpha_i = 4\pi abc \frac{\epsilon_{NP} - \epsilon_m}{3\epsilon_m + 3L_i(\epsilon_{NP} - \epsilon_m)} \quad (16)$$

where L_i is the geometrical factor of the ellipsoid. According to Eq. 16, the spheroidal NP exhibits two spectrally separated plasmon resonances, corresponding to conduction electron oscillations along the minor or major axis. The main question here is, why two LSPR peaks appear only for prolate with large AR, while there is one prominent peak in the absorption spectra of NPs with the oblate or prolate shape with small AR. To answer this question, the polarizability of spheroidal core-shell NPs is analyzed (Eq. 1). Based on Eq. 1, the polarizability of a spheroid is extremely sensitive to both core and shell geometrical factor.

In this regard, the core and shell depolarization factors and the polarizabilities of $\text{Fe}_3\text{O}_4@Au$ along minor and major axis (i.e., α_1 and α_2) are calculated. Fig. 6 provides a clear comparison be-

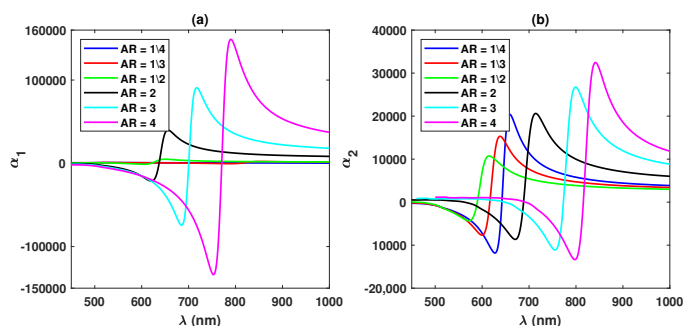


Fig. 6 Polarizability of $Fe_3O_4@Au$ along (a) minor axis α_1 and (b) major axis α_2 .

tween α_1 and α_2 of spheroidal $Fe_3O_4@Au$ with different aspect ratios. For prolate geometry, the polarizability along the major axis is stronger than the one along the minor axis (i.e. $\alpha_1 > \alpha_2$). Fig. 6(b) denotes that the polarizability of all NP including prolate and oblate meet the resonance condition. In contrary, the strength of polarizability of oblate along the minor axis is higher than the polarizability along the major axis (i.e. $\alpha_1 < \alpha_2$). In the case of small oblates, the α_1 is too small ($\alpha_1 \approx 0$) and the corresponding peak in the absorption spectrum is hardly distinguished (Fig. 6(a)). Consequently, two peaks appear in the spectrum by considering average polarizability. It is noteworthy that although both polarizabilities of prolate NP with $AR = 2$ are non-zero, their resonant wavelengths are very close and overlap with each other. The result appears as broadening of absorption spectrum. Since there is a similar trend for $Fe_3O_4@Ag$, the relevant explanations are ignored to avoid repetition.

3.4 Core Size Effect.

As mentioned before, any variation in f , either by changing the core radius or by changing the shell thickness, leads to absorption spectrum modification. To exemplify the effect of the core size, the core-shell NPs are set with a fixed shell thickness of 4 nm, whereas the values of minor radius (a) is increased from 6 nm to 12 nm. These calculations are performed for three kinds of spheroid. The absorption spectra of $Fe_3O_4@Au$ and $Fe_3O_4@Ag$ core-shell NPs with the shape of sphere ($AR = 1$), oblate ($AR = \frac{1}{3}$) and prolate ($AR = 3$) dispersed in the polymer with different core size and same shell thickness are shown in Fig. 7.

It is clearly observed that by increasing the core size of $Fe_3O_4@Au$, the LSPR peak is redshifted and the absorption efficiency is intensified. As a result, light energy conversion to heat is improved. This improvement is remarkable for sphere and oblate, while the increase in the amount of absorption is lower for the prolate. It can be said that as f increases, the absorption efficiency increases and resonance occurs at lower frequencies. The tuning possibility of the peak position could be controlled from 600 nm to 710 nm, 580 nm to 670 nm and 750 nm to 950 nm for sphere, oblate and prolate, respectively, when the magnetite radius increases from $a = 6$ nm to $a = 12$ nm.

As illustrated in Fig. 7(d)-(f), with increasing core size of $Fe_3O_4@Ag$ NPs, the resonance peak of BM shows a considerable

redshift, whereas ABM resonance exhibits a slight blueshift. In comparison with gold shell, there is a slight improvement in the absorption efficiency of NPs with silver shell. However, this efficiency is still much higher than the gold yield. It could be concluded that the LSPR position of silver coated NPs is more tunable, while the amount of generated heat is almost constant. The bonding LSPR position for sphere ($AR = 1$), oblate ($AR = \frac{1}{3}$) and prolate ($AR = 3$) can be changed from 500 nm to 610 nm, 480 nm to 575 nm and 670 nm to 875 nm, respectively, when the minor radius of magnetite increases from 6 nm to 12 nm. It is worth mentioning that one of the transparency spectral windows of human tissues is 700 nm - 900 nm⁵⁵. Therefore, the prolate silver and gold coated NPs could be expected to be ideal candidates for photothermal applications due to their resonance positions.

It is also instructive to analyze the behavior of LSPR displacement for NPs with different aspect ratios ranging from 0.25 to 4. The results summarized in Table. 1 show the similar trend and reveal that BM peak of sphere, oblate and prolate NPs move toward the longer wavelength, as the core: shell ratio increases and its value enhances as well. The important outcome is that stretching the sphere leads to the redshift of the peak, while the blueshift of LSPR peak is observed by flattening the sphere. Further, the second peak appears in the prolate NPs with large aspect ratio (i.e., $AR = 3$ and 4), but there is no additional peak in small prolate (i.e., $AR = 2$) and oblate NPs.

3.5 Shell Thickness Effect.

To control and tune the absorption efficiency and peak position, the spectra of core-shell NPs with different shell thickness have also been discussed. Fig. 8 compares the absorption spectra of different shapes of $Fe_3O_4@Au$ and $Fe_3O_4@Ag$ with fixed core diameter and different shell thickness.

In the case of $Fe_3O_4@Au$ NPs, the results clearly demonstrate how the LSPR peak gets blueshifted and absorption efficiency is intensified as outer shell thickness of NP increases. This trend is also observed for oblate and prolate NPs. For $Fe_3O_4@Ag$, the resonance peak for BM exhibits a significant blueshift, while the resonance peak for ABM shows a slight redshift as the thickness of silver is increased. The same trend is observed for three kind of NP shapes.

Similarly, the effect of shell thickness on NPs with different aspect ratios ranging from 0.25 to 4 is also analyzed. The results reported in Table. 2 signify that the shell thickness is an important parameter for tuning the resonance in the wavelength range from 300 to 1400 nm.

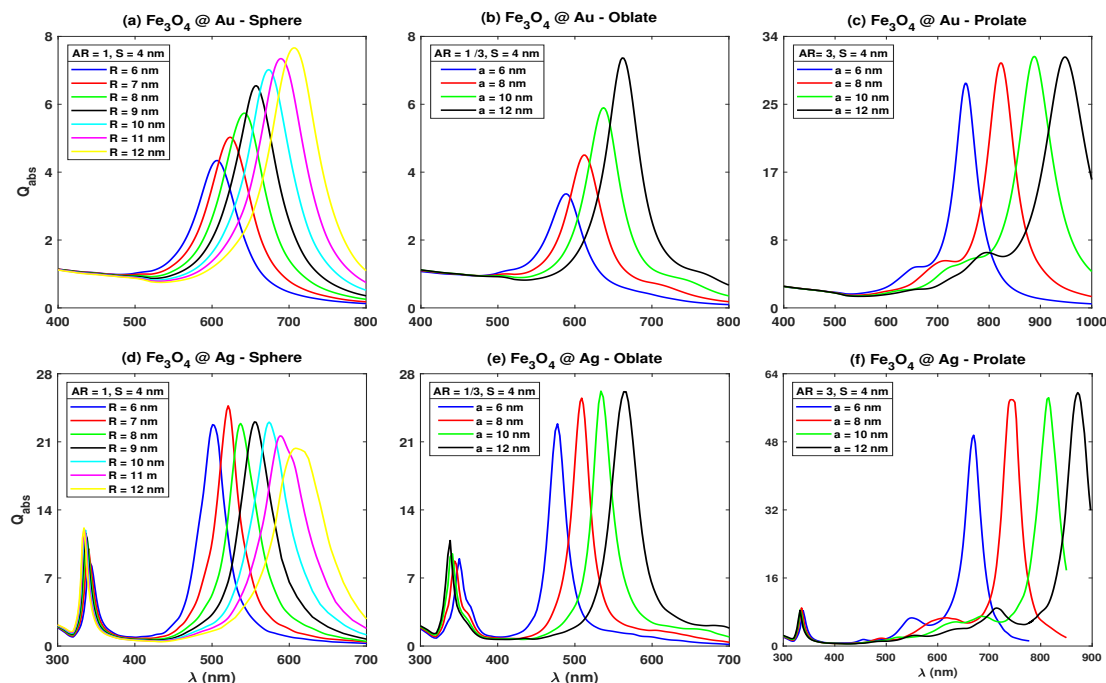


Fig. 7 Effect of core size on the absorption spectra of $Fe_3O_4@Au$ and $Fe_3O_4@Ag$ NPs with different aspect ratios.

Table 1 Summary of LSPR peaks of core-shell NPs of various shape and core size (The metal shell of all NPs is fixed at 4 nm)

Shape AR	Core Diameter (nm)	BM $Fe_3O_4@Au$	New Peak	BM, $Fe_3O_4@Ag$	ABM $Fe_3O_4@Ag$	New Peak
Sphere $AR = 1$	12	8.64 @ 607	—	22.80 @ 500	8.48 @ 342	—
	16	11.44 @ 641	—	22.88 @ 536	11.12 @ 338	—
	20	14.80 @ 673	—	23.04 @ 574	11.92 @ 336	—
	24	15.36 @ 707	—	20.40 @ 608	12.16 @ 334	—
Oblate $AR = \frac{1}{2}$	12	6.64 @ 593	—	19.92 @ 480	8.24 @ 350	—
	16	8.64 @ 619	—	21.36 @ 514	8.56 @ 344	—
	20	11.04 @ 647	—	20.48 @ 545	10.24 @ 339	—
	24	13.12 @ 673	—	21.92 @ 575	10.72 @ 335	—
Oblate $AR = \frac{1}{3}$	12	6.72 @ 589	—	19.92 @ 480	8.24 @ 350	—
	16	9.04 @ 613	—	21.36 @ 514	8.48 @ 344	—
	20	11.76 @ 637	—	20.48 @ 545	10.24 @ 339	—
	24	14.72 @ 661	—	21.84 @ 575	10.72 @ 335	—
Oblate $AR = \frac{1}{4}$	12	7.12 @ 587	—	25.60 @ 475	9.52 @ 350	—
	16	9.84 @ 609	—	30.64 @ 505	9.12 @ 344	—
	20	12.96 @ 633	—	30.40 @ 530	9.68 @ 341	—
	24	16.96 @ 657	—	32.48 @ 557	11.28 @ 338	—
Prolate $AR = 2$	12	17.36 @ 669	—	30.08 @ 537	7.12 @ 338	1.12 @ 430
	16	20.56 @ 722	—	29.52 @ 631	8.48 @ 335	1.28 @ 456
	20	21.44 @ 769	—	31.12 @ 686	8.40 @ 332	1.60 @ 483
	24	22.08 @ 81	—	36.80 @ 733	8.72 @ 332	1.76 @ 507
Prolate $AR = 3$	12	28.16 @ 754	—	49.60 @ 670	8.32 @ 338	6.64 @ 548
	16	30.64 @ 822	—	57.92 @ 742	8.96 @ 335	6.64 @ 616
	20	31.52 @ 888	—	58.40 @ 815	8.48 @ 332	6.96 @ 685
	24	31.44 @ 947	—	59.60 @ 872	8.32 @ 332	8.96 @ 714
Prolate $AR = 4$	12	37.12 @ 842	3.92 @ 663	82.01 @ 760	8.80 @ 338	5.36 @ 561
	16	37.76 @ 932	4.24 @ 705	72.32 @ 858	8.80 @ 334	5.04 @ 609
	20	37.60 @ 1015	5.04 @ 767	78.96 @ 937	8.64 @ 332	6.08 @ 696
	24	36.10 @ 1091	5.84 @ 798	72.96 @ 1015	8.32 @ 332	8.08 @ 722

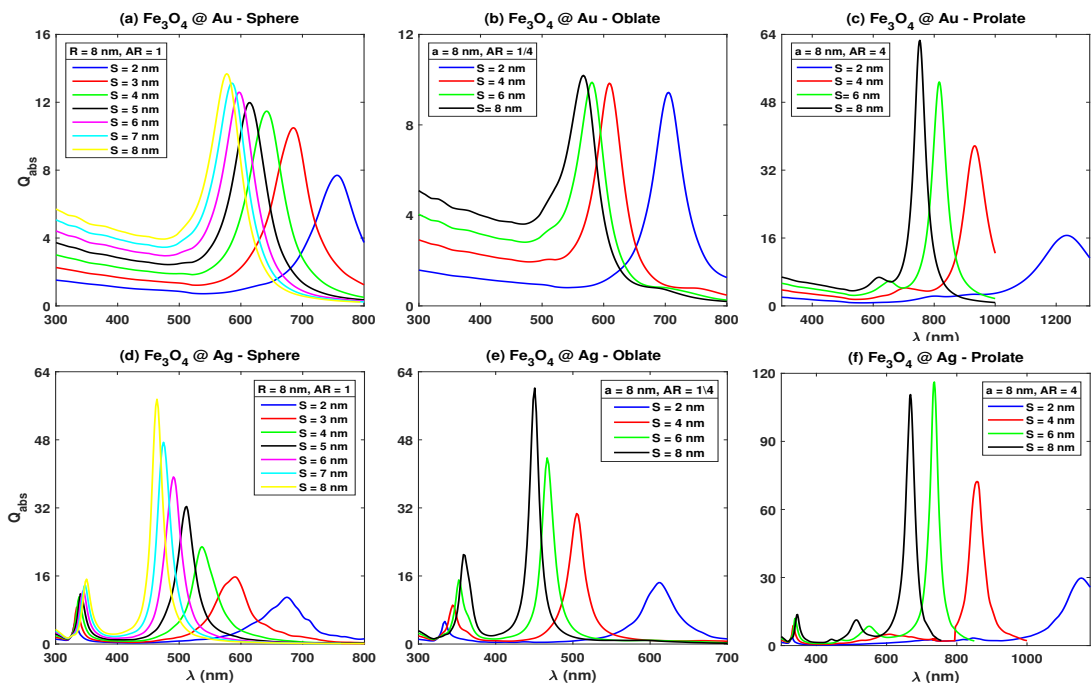


Fig. 8 Effect of shell thickness on the absorption spectra of $Fe_3O_4@Au$ and $Fe_3O_4@Ag$ NPs with different aspect ratios.

Table 2 Summary of LSPR peaks of core-shell NPs of various shape and shell thickness (For all NPs, $a = 8$ nm.)

Shape	Shell Thickness	BM	New Peak	BM,	ABM	New Peak
AR	(nm)	$Fe_3O_4@Au$		$Fe_3O_4@Ag$	$Fe_3O_4@Ag$	
Sphere	2	7.68 @ 756	—	10.96 @ 673	5.44 @ 332	—
	4	11.44 @ 641	—	22.88 @ 537	11.04 @ 338	—
	6	12.01 @ 597	—	39.28 @ 491	12.41 @ 344	—
	8	13.68 @ 577	—	57.68 @ 464	15.22 @ 350	—
Oblate	2	6.81 @ 724	—	9.28 @ 633	5.36 @ 334	—
	4	8.64 @ 619	—	21.36 @ 514	8.48 @ 344	—
	6	9.52 @ 585	—	33.04 @ 473	13.12 @ 352	—
	8	10.21 @ 569	—	49.68 @ 453	18.08 @ 360	—
Oblate	2	8.24 @ 710	—	12.24 @ 615	5.36 @ 334	—
	4	8.96 @ 613	—	25.44 @ 508	8.72 @ 344	—
	6	9.52 @ 581	—	39.52 @ 468	14.32 @ 352	—
	8	10.01 @ 567	—	57.61 @ 450	20.40 @ 360	—
Oblate	2	9.44 @ 706	—	14.48 @ 611	5.28 @ 334	—
	4	9.84 @ 609	—	30.64 @ 505	9.12 @ 344	—
	6	9.92 @ 581	—	43.68 @ 467	15.04 @ 352	—
	8	10.16 @ 567	—	60.16 @ 450	20.96 @ 358	—
Prolate	2	10.02 @ 898	—	15.68 @ 835	3.76 @ 330	—
	4	20.56 @ 722	—	29.60 @ 631	8.48 @ 335	—
	6	24.08 @ 653	—	46.80 @ 556	9.99 @ 341	—
	8	23.76 @ 619	—	63.52 @ 521	12.39 @ 347	—
Prolate	2	13.59 @ 1067	2.64 @ 792	25.20 @ 985	3.68 @ 329	—
	4	30.64 @ 822	5.84 @ 710	57.92 @ 742	8.96 @ 335	6.64 @ 616
	6	39.59 @ 733	7.52 @ 648	65.12 @ 646	10.8 @ 341	9.59 @ 542
	8	34.96 @ 682	6.48 @ 603	66.08 @ 587	10.1 @ 347	10.08 @ 504
Prolate	2	16.79 @ 1230	2.24 @ 791	29.59 @ 1155	3.76 @ 330	3.28 @ 845
	4	37.76 @ 932	4.24 @ 706	72.32 @ 858	8.79 @ 334	4.96 @ 609
	6	52.88 @ 816	5.84 @ 653	115.9 @ 736	11.98 @ 340	8.48 @ 551
	8	62.56 @ 753	6.72 @ 619	110.4 @ 668	13.68 @ 346	11.28 @ 514

4 Conclusion

In this work, the optical properties of $Fe_3O_4@Au$ and $Fe_3O_4@Ag$ core-shell NPs have been explored using the Discrete Dipole Approximation method. Magneto-plasmonic core-shell structures merge the LSPR properties of silver or gold NPs and magnetic features of Fe_3O_4 in a single NP. Compared to a homogeneous NP, the core-shell NPs provide high tunability in the LSPR position by manipulating the filling factor, core size and shell thickness.

In comparison with pure Au, the absorption spectrum of $Fe_3O_4@Au$ shows more intense redshifted peak (BM). Results indicate that an increase in magnetic core radius corresponds to a shift of the BM peak to longer wavelength, however, an increase in the shell thickness leads to move the peak to shorter wavelengths.

It is also found that two resonance peaks exist in the absorption spectrum of $Fe_3O_4@Ag$. They can be attributed to two different LSPR modes in the NP; the blueshifted antibonding mode with energy concentration at magnetite-silver interface and redshifted bonding mode at silver-polymer interface. Double LSPR modes together with wide tunability make $Fe_3O_4@Ag$ a good candidate for applications where two or more simultaneous absorption enhancement at different wavelengths is required. These two modes exhibit opposite trends in moving the peak position, either redshift or blueshift, when the core radius or shell thickness is varied. An increase in magnetic core radius or decrease in the shell thickness leads to remarkable BM peak redshift together with the slight blueshift of ABM mode. It is also observed that the absorption efficiency for $Fe_3O_4@Ag$ is higher than $Fe_3O_4@Au$. Higher absorption leads to higher temperature increase, when $Fe_3O_4@Ag$ NP is illuminated at its LSPR wavelength.

More significant modifications in the absorption spectra have been observed when the spherical shape of NP is changed to oblate and prolate. When the spherical NP becomes oblate, the bonding mode of both $Fe_3O_4@Au$ and $Fe_3O_4@Ag$ shifts towards shorter wavelengths and the $Fe_3O_4@Ag$ antibonding mode shows a blueshift. As the geometry of NP changes to prolate, the mentioned modes experience opposite shift. Based on these results, the absorption efficiency of both $Fe_3O_4@Au$ and $Fe_3O_4@Ag$ is noticeably enhanced as the NP shape changes to the prolate. Therefore, NPs with prolate shape are much more efficient absorber than oblate or spherical NPs. Furthermore, the new peak appears in the absorption spectra of prolate NPs with large aspect ratio due to the symmetry breaks down. As the geometry of NP becomes asymmetric, the polarization of NP is no longer homogeneous. Therefore, multipolar excitation arises and new peaks appear in the absorption spectra for large NPs.

Notes and references

- 1 J. R. Mejía-Salazar and O. N. Oliveira, *Chemical Reviews*, 2018, **118**, 10617–10625.
- 2 A. G. Brolo, *Nature Photonics*, 2012, **6**, 709–713.
- 3 M. B. Gawande, A. Goswami, T. Asefa, H. Guo, A. V. Biradar, D. L. Peng, R. Zboril and R. S. Varma, *Chem. Soc. Rev.*, 2015, **44**, 7540–7590.
- 4 S. Lal, S. E. Clare and N. J. Halas, *Acc Chem Res*, 2008, **41**, 1842–1851.
- 5 Z. Fan, M. Shelton, A. K. Singh, D. Senapati, S. A. Khan, and P. C. Ray, *ACS Nano*, 2012, **6**, 1065–1073.
- 6 S. Wang, H. Xu and J. Ye, *Phys. Chem. Chem. Phys.*, 2014, **16**, 12275.
- 7 N. Hadilou, A. Navid-Khoshgenab, M. Amoli-Diva and R. Sadighi-Bonabi, *J. Pharm. Sci.*, 2018, **107**, 3123–3133.
- 8 M. Amoli-Diva, R. Sadighi-Bonabi, K. Pourghazi and N. Hadilou, *J. Pharm. Sci.*, 2018, **107**, 2618–2627.
- 9 E. Yan, Y. Ding, C. Chen, R. Li, Y. Hu and X. Jiang, *Chem. Commun.*, 2009, **19**, 2718–2720.
- 10 G. Baffou, R. Quidant and C. Girard, *Appl. Phys. Lett.*, 2009, **94**, 153109.
- 11 A. O. Govorov and H. Richardson, *Nano Today*, 2007, **2**, 30–38.
- 12 N. Dalong, B. Wenbo, B. E. Emily, C. Weibo and S. Jianlin, *Chem. Soc. Rev.*, 2017, **46**, 7438–7468.
- 13 A. S. Arbab, L. A. Bashaw, B. R. Miller, E. K. Jordan, B. K. Lewis, H. Kalish and J. A. Frank, *Radiology*, 2003, **229**, 838–846.
- 14 H. Peng, Y. Lingjie, Z. Ahui, G. Chenyi and Y. Fangli, *J. Phys. Chem. C*, 2009, **113**, 900–906.
- 15 M. Gema, P. Ernesto, C. Teresa and P. Carmen, *J. Phys. Chem. C*, 2011, **115**, 25247–25256.
- 16 M. F. Casula, Y. wook Jun, D. J. Zaziski, E. M. Chan, A. Corrias and A. P. Alivisatos, *J. Am. Chem. Soc.*, 2006, **128**, 1675–1682.
- 17 R. Sharma, S. Roopak, Pathak and et al., *Plasmonics*, 2017, **12**, 977–986.
- 18 L. León-Félix, J. Coaquira, M. Martínez, G. F. Goya, J. Mantilla, M. H. Sousa, L. S. Valladares, C. Barnes and P. C. Moraes, *Scientific Reports*, 2017, **7**, 1–8.
- 19 A. Sheverdin and C. Valagiannopoulos, *Phys. Rev. B*, 2019, **99**, 075305.
- 20 P. K. Jain, K. S. Lee, I. H. El-Sayed and M. A. El-Sayed, *J. Phys. Chem. B.*, 2006, **110**, 7238–7248.
- 21 E. Prodan and P. Nordlander, *Nano Letters*, 2003, **3**, 543–547.
- 22 V. G. Stolerua and E. Toweb, *Appl. Phys. Lett.*, 2004, **85**, 5152.
- 23 A. Bansal, J. S. Sekhon and S. S. Verma, *Plasmonics*, 2014, **9**, 143.
- 24 W. Wang, J. Luo, Q. Fan, M. Suzuki, I. S. Suzuki, M. H. Engelhard, Y. Lin, N. Kim, J. Q. Wang and C.-J. Zhong, *J. Phys. Chem. B*, 2005, **109**, 21593–21601.
- 25 C. S. Levin, C. Hofmann, T. A. Ali, A. T. Kelly, E. Morosan, P. Nordlander, K. H. Whitmire and N. J. Halas, *ACS Nano*, 2009, **3**, 1379–1388.
- 26 C. Zhang, B.-Q. Chen, Z.-Y. Li, Y. Xia and Y.-G. Chen, *J. Phys. Chem. C.*, 2015, **119**, 16836–16845.
- 27 W. Zhang, H. Ma and J. Fan, *Plasmonics*, 2019, **14**, 1123–1129.
- 28 C. F. Bohren and D. R. Huffman, *Absorption and Scattering of Light by Small Particles*, (Wiley-VCH, 2008).
- 29 S. A. Maier, *Plasmonics: Fundamentals and Applications*, (Springer, 2004).

- 30 M. Arnold, M. Blaber and M. Ford, *Opt. Express*, 2009, **17**, 3835.
- 31 R. Sharma, S. Roopak, N. kumar Pathak, R. Uma and R. P. Sharma, *Plasmonics*, 2017, **13**, 335–343.
- 32 V. Amendola, *Phys. Chem. Chem. Phys.*, 2016, **18**, 2230–2241.
- 33 B. T. Draine, *J. Opt. Soc. Am. A*, 1994, **11**, 1491.
- 34 B. T. Draine and J. J. Goodman, *Astrophys. J.*, 1993, **405**, 685–697.
- 35 A. L. Gonzalez, C. Noguez, G. P. Ortiz and Rodriguez-Gattorno, *J. Phys. Chem. B*, 2005, **109**, 17512–17517.
- 36 E. M. Purcell, *Electricity and Magnetism*, (McGraw-Hill: New York, 1963).
- 37 E. M. Purcell and C. R. Pennypacker, *Astrophys. J.*, 1973, **186**, 705–714.
- 38 P. J. Flatau and B. T. Draine, *Optics Express*, 2012, **20**, 1247–1252.
- 39 P. J. Flatau and B. T. Draine, *Optics Express*, 2014, **22**, 21834–21846.
- 40 P. C. Chen, S. C. Mwakwari and A. K. Oyeler, *Nanotechnol Sci Appl.*, 2008, **1**, 45–66.
- 41 C. R. Patra, R. Bhattacharya, D. Mukhopadhyay and P. Mukherjee, *Advanced Drug Delivery Reviews*, 2010, **62**, 346–361.
- 42 S. Kessentini and D. Barchiesi, *Biomed. Opt. Express*, 2012, **3**, 590–604.
- 43 U. Kreibig and M. Vollmer, *Optical Properties of Metal Clusters*, (in: Springer Ser. Mater. Sci, Springer, Berlin, 1995).
- 44 C. Noguez, *The Journal of Physical Chemistry C*, 2007, **111**, 3806–3819.
- 45 W. Z. Wang, M. Y. Wan, Z. L. Hua, Yin, X. Chang, Yi and M. Fang, *Optics Communications*, 2019, **439**, 66–75.
- 46 M. Farokhnezhad and M. Esmaeilzadeh, *The Journal of Physical Chemistry C*, 2019, **123**, 28907–28918.
- 47 P. B. Johnson and R. W. Christy, *Phys. Rev. B*, 1972, **6**, 4370–4379.
- 48 A. Schlegel, S. F. Alvarado and P. Wachter, *Journal of Physics C: Solid State Physics*, 1979, **12**, 1157–1164.
- 49 M. A. Ordal, R. J. Bell, R. W. Alexander, L. L. Long and M. R. Query, *Appl. Opt.*, 1985, **24**, 4493–4499.
- 50 E. Prodan, C. Radloff, N. J. Halas and P. Nordlander, *Science*, 2003, **302**, 419–422.
- 51 M. Arnold, M. Blaber and M. Ford, *Opt. Express*, 2014, **22**, 3186–3198.
- 52 J. Qian, Y. Li, J. Chen, J. Xu and Q. Sun, *J. Phys. Chem. C*, 2014, **118**, 8581–8587.
- 53 U. K. Chettiar and N. Engheta, *Opt. Express*, 2012, **20**, 22976.
- 54 E. R. Encina and E. A. Coronado, *J. Phys. Chem. C*, 2016, **120**, 5630–5639.
- 55 G. Baffou, R. Quidant and C. Girard, *Appl. Phys. Lett.*, 2009, **94**, 153109.